Materials and Design 190 (2020) 108551

Contents lists available at ScienceDirect

Materials and Design

journal homepage: www.elsevier.com/locate/matdes

# *In-situ* investigation of crystallization and structural evolution of a metallic glass in three dimensions at nano-scale

Bo Chen [a,b,c,*], Jiecheng Diao [a,b], Qiang Luo [d,**], Jonathan Rawle [e], Xianping Liu [a,f], Chris Nicklin [e], Jun Shen [a], Ian Robinson [b,a,***]

[a] School of Materials Science and Engineering, Tongji University, Shanghai 201804, China
[b] London Centre for Nanotechnology, University College London, London WC1H 0AH, UK
[c] Key Laboratory of Performance Evolution and Control for Engineering Structures of the Ministry of Education, Tongji University, Shanghai 200092, China
[d] School of Materials Science and Engineering, Southeast University, Nanjing 211189, China
[e] Diamond Light Source, Harwell Campus, Oxfordshire OX11 0DE, UK
[f] Key Laboratory of Advanced Civil Engineering Materials (Tongji University), Ministry of Education, Shanghai 201804, China

## HIGHLIGHTS

- The growth and strain variation of individual crystals in the Fe-based metallic glass during annealing were investigated.
- The crystal growth follows a two-step model with the growth of both the crystal core and fractal structure.
- There is preferential growth along the surface of specimen during the α-Fe crystal formation from the metallic glass.
- Growth stagnation and strain relaxation are observed in the grown crystals while cooling.

## GRAPHICAL ABSTRACT

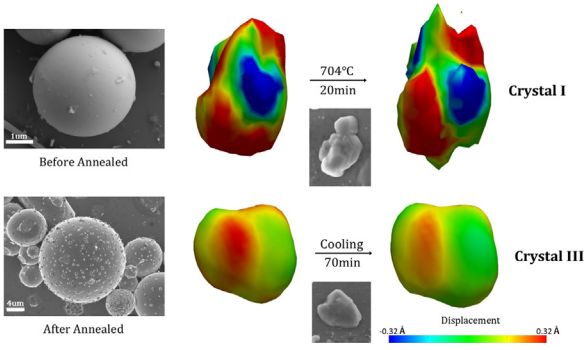


## ARTICLE INFO

*Article history:*
Received 12 December 2019
Received in revised form 29 January 2020
Accepted 4 February 2020
Available online 04 February 2020

*Keywords:*
Fe-based metallic glass (MG)
Two-step crystal formation
Bragg coherent X-ray diffraction imaging (BCDI)
Three-dimensional (3D) strain mapping
Fractal structure

## ABSTRACT

The crystallization behaviour of metallic glasses (MGs) has been investigated since the discovery of these important functional materials in order to optimize their synthesis procedures and improve their performances. Methods including powder X-ray diffraction and transmission electron microscopy are usually combined to characterize the crystalline structure in these "amorphous" materials. Until now, these methods, however, have failed to show the crystallization of individual crystals in three dimensions. In this work, *in-situ* Bragg coherent X-ray diffraction imaging (BCDI) reveals the growth and the strain variation of individual crystals in the Fe-based MGs during annealing. There is preferential growth along the surface of the MG sample particles during the crystal formation and fractal structure formation around the developing crystal surfaces; there is also strain relaxation happening from the inner parts to the surfaces of the developing crystals while cooling. The work leads to propose that during the crystallization of Fe-based MGs, the growth of the individual crystals follows a two-step procedure; and at higher temperature after the first crystallization period of the Fe-based MGs, the

* Correspondence to: Bo Chen, School of Materials Science and Engineering, Tongji University, Shanghai 201804, China.
** Corresponding author.
*** Correspondence to: Ian Robinson, London Centre for Nanotechnology, University College London, London WC1H 0AH, UK.
*E-mail addresses:* bo.chen@tongji.edu.cn (B. Chen), q.luo@seu.edu.cn (Q. Luo), i.robinson@ucl.ac.uk (I. Robinson).

https://doi.org/10.1016/j.matdes.2020.108551

crystallization of α-Fe could be a competitive process between the growth of α-Fe crystals and the erosion from other elements.



## 1. Introduction

The crystallization phenomenon in metallic glass (MG) has attracted tremendous attention, not only because of the interests in developing MG composites with better performances [1,2], but also in seeking critical insights of this complex material transformation process [3–7]. Regarding the mechanical properties of these materials, MG can provide great strength under high compression since there are few defects and no grain boundary within them. Indeed, some bulk metallic glasses (BMGs) can survive up to 5GPa or even higher compression [8,9]. Under tension, some MGs have excellent elastic strain which could exceed 2% [10,11]. However, their lack of macroscopic plastic strain hinders the application of MGs as a general structural material. Most of the MG materials are also brittle in tension due to the lack of barriers for crack propagation and constraints for shear band propagation within them [12–14]. However, introduction of reinforcing crystalline phase in the MG materials could substantially improve their global plasticity by promoting the generation of multiple shear bands and diverting the inhomogeneous flow in the MGs which makes the MG materials a suitable candidate for engineering applications. The (partial) crystallized regions in the amorphous matrix could also influence their magnetic properties. For example, the magnetocaloric effect is widely found in rare-earth (RE)-based MGs which are promising for using as magnetic refrigerants. The nano-clusters or nano-scale precipitation with crystalline grains embedded in the amorphous matrix lead to an almost-constant, relatively high magnetic-entropy change which favors the Ericsson cycle [15]. Other properties such as multiple spin glass behavior may also be a result of nano-scale nucleation [13]. Compared with the amorphous or crystalline materials, partially crystallized MG composites show unique mechanical and magnetic properties [16,17]. Therefore, it is essential to investigate the relationship between the properties of MGs and their crystallization behaviour or structure which includes, for example, the crystal size and strain distribution within the nano-crystalline materials.

Currently, the crystallization behaviour of the MGs at the nanometer length scale is still somewhat badly known. This is partially because of the lack of available characterization methods, which has led to almost no means for direct studies on the crystallization and growth of individual crystal grains in the MG materials.

Coherent X-ray diffraction imaging (CDI) is a lens-less imaging method, which utilizes the high coherence of X-rays generated from synchrotron radiation facilities or X-ray free electron lasers (XFELs) [18]. Lenses are avoided in CDI by replacing them with computational image reconstruction algorithms. With nearly 20 years of development, various types of CDI have been proposed, and they have been applied to different specimens [19–24].

Bragg CDI (BCDI) is a specific X-ray imaging approach for nano- and micro-crystals, in which a coherent incident wave is chosen to illuminate the samples and a tilting series of far-field diffraction patterns is measured around a selected Bragg angle [25,26]. BCDI has been successfully applied to reveal some key physics and materials phenomena such as atom diffusion and rearrangement in alloys [27,28], charging and discharging of battery materials [29,30] and crystal growth behaviour [31,32]. BCDI experimental set-up can remove the non-crystalline signals that are scattered in other directions, and can select the targeted crystals by their corresponding Bragg diffraction peaks. The measured Bragg diffraction patterns are the Fourier transform of the three-dimensional (3D) density distributions of the illuminated crystals, in which the amplitude can be directly measured and the phase needs to be recovered by iterative mathematic algorithms [33,34]. The reconstructed amplitude images, representing the Bragg electron density distribution of the specimens, define the shape of crystals in three dimensions with a spatial resolution of typically around 20 nm. If each crystal in a composite is oriented differently they can be imaged separately, so are easily segmented from their neighbours. In addition, the reconstructed phase images encode the atomic displacement field through its projection onto the momentum transfer vector, $Q = k_f - k_i$, where $k_f$ and $k_i$, are the exit and incident wavevectors, respectively. The displacement field can be converted into a strain map within the measured crystal, which is a powerful tool for investigating the internal structures of individual crystals.

As BCDI is generally a non-destructive imaging method and is sensitive to crystalline materials, in this work we used BCDI to investigate the crystallization process of an Fe-based MG in three dimensions at the nano-scale by an *in-situ* approach. The chosen material of interest is $Fe_{49.7}Cr_{18}Mn_{1.9}Mo_{7.4}W_{1.6}B_{15.2}C_{3.8}Si_{2.4}$ MG powders, which is a good candidate for making anti-corrosive coatings or for using as the feedstock powders in high velocity oxygen fuel (HVOF) spraying [35]. Additionally, some products of crystallized Fe-based MGs such as the Fe-based nano-crystalline alloys have already been widely used because of their excellent soft magnetic properties. The target Fe-based MG powder specimens were heated to their crystallization temperature in vacuum during the *in-situ* BCDI measurements so that the crystallization behaviour of the materials could be recorded. This article reports the main results of our study that there is preferential growth in a specific direction in the individual crystals during heating and that a fractal structure around the crystal surface was observed. We also discovered a significant strain relaxation in the grown crystals during the subsequent cooling process without change in the crystal shape. A two-step crystallization model during the crystal growth of the Fe-based MG materials under heating is suggested from the results of this work.

## 2. Experimental methods

The powders of $Fe_{49.7}Cr_{18}Mn_{1.9}Mo_{7.4}W_{1.6}B_{15.2}C_{3.8}Si_{2.4}$ MG were made *via* the high-pressure Argon gas atomization method, in which mixtures of different elements in the designed ratio were induction-melted in an Argon gas atmosphere. Inert gas jets were used to atomize the molten powders into small droplets that formed into powders afterwards for various measurements.

The powder XRD measurement of the MG samples, both the as-received and annealed ones, were done by a Bruker D8 Advance powder X-ray diffractometer using Cu Kα radiation of 0.1542 nm wavelength (/ X-rays with 8.04 keV energy) with the working voltage of 40 kV and the working current of 40 mA at the scanning speed of 2°/min.

The size distribution of the samples was measured by a Beckman Coulter laser particle analyzer LS230. The differential scanning calorimetry (DSC) measurement was carried out by an SDT Q600 machine (from TA Instruments), the simultaneous DSC-TGA (differential scanning calorimetry-thermogravimetric analysis) instrument, in an Argon atmosphere with a gas flow of 50 mL/min at a heating rate of 20 K/min. The electron micrographs and EDS mappings of the samples were obtained from a Zeiss Sigma 300VP SEM with an Oxford AZtec X-Max 80 EDS. Selected area electron diffraction (SAED) was carried out by a JOEL JEM-2100 TEM at 200 kV accelerating voltage.

The *in-situ* BCDI experiments were carried out at the beamline I-07 of Diamond Light Source (DLS), the UK. The as-received MG powders were ultrasonically dispersed in tetraethyl orthosilicate (TEOS)-ethanol

solution with the ratio of 1:75 (in volume), then this suspension was drop-cast on a silicon wafer. The suspension was heated in air at about 200°C for half an hour to be dried to convert the TEOS liquid into a vitreous $SiO_2$ network which can bond the sample powders and the Si wafer together. Then, these as-fixed samples were mounted on the sample stage and load-locked into the vacuum chamber at the beamline I-07 of the DLS which had a base pressure of $2 \times 10^{-10}$ mbar inside. The samples were centered on the rotation axis of the diffractometer, then heated *in-situ* by electron bombardment in the vacuum chamber while a coherent 9 keV X-ray beam illuminated the samples upon heating for measurements. The centre part of the X-ray beam with the size of 20 μm × 20 μm was selected for illumination by a group of slits. The illumination beam is coherent over the lateral dimensions of the sample because of the high brightness of the DLS and in the longitudinal direction by virtue of its Si(111) monochromator. For all the BCDI measurements, the sample-detector distance was kept at 1.52 m. The Pilatus 100K detector of 487 × 195 pixels with pixel size of 172 μm × 172 μm has been used to record the diffraction patterns of the annealing samples. For recording the full 3D Bragg diffraction patterns of the α-Fe crystals, once a diffraction pattern with strong signals was found at the right Bragg angle on the detector, around $2\theta = 39.7°$ in the reported work. The growing crystal was then centered in the X-ray beam, in the XY plane and along the tilting and rotation directions, to peak up its diffraction. It was then rotated through its whole Bragg diffraction peak, usually by 0.4°, with a step size of 0.005°. This allows the individual speckles around the centre of the diffraction pattern can be recorded in at least 2 rotation angles, *i.e.* 2 slice images of the whole diffraction pattern to satisfy the over-sampling condition. At each rotation angle, a two-dimensional (2D) slice of the Bragg diffraction pattern of the crystal was recorded on the Pilatus detector with an exposure time of 10 s or 30 s depending on the diffraction intensity from the crystal. These 2D diffraction slices were then stacked together to form a full 3D Bragg diffraction pattern which was used for real-space image reconstruction.

After the BCDI experiments, these annealed samples were removed from the beamline vacuum chamber and kept for the later measurement by SEM *etc.*

## 3. Results and discussion

### 3.1. Characteristics of the as-received samples

Fig. 1a shows a powder X-ray diffraction (XRD) pattern of the Fe-based MG samples in their starting state as received. The inset at the top-right corner of Fig. 1a is a selected area electron diffraction (SAED) pattern of the same sample from transmission electron microscope (TEM). A broad peak between 30° and 60° (2θ values) can be seen whilst there are no sharp diffraction features present in the powder XRD pattern, which indicates that the sample can be identified as an amorphous material. This is confirmed by its SAED pattern that shows only isotropic scattering rings without any distinct diffraction spots. The size distribution profile of the as-received sample in Fig. 1b shows that there are a great number of particles between 2 μm and 10 μm. Synchrotron X-rays with an energy of 9 keV were selected for our BCDI measurements. These X-ray photons have an 8 μm penetration depth into this Fe-based MG, which is sufficient to illuminate a large portion of individual MG particles in this sample. Fig. 1c presents the DSC curve of the sample measured with a heating rate of 20 K/min in an Argon atmosphere. There are two exothermic peaks at 683°C and 772°C. These two split exothermic peaks indicate 2 heat releasing processes, which is consistent with a two-stage crystallization process [36–38] having occurred in the chosen type of MG samples.

Fig. 1d and e are scanning electron microscope (SEM) micrographs of the as-received MG powder sample used for the *in-situ* BCDI measurements, in which Fig. 1e is a zoomed-in image of the yellow square region in Fig. 1d. The SEM micrographs show the as-received MG particles are well-shaped spheres with smooth surfaces before the *in-situ* X-ray measurements. The sizes of these particles range from 2 μm to 5 μm. The energy dispersive spectrometer (EDS) measurement result from a point on an MG particle (indicated by a yellow dot in Fig. 1e) is shown in Fig. 1f. The result gives a similar chemical composition as expected from the synthesis, although there are noticeable differences in the expected proportions of C and B. The EDS result shows 14.2 at.% of C and there is no signal for B, while the chemical formula from synthesis has

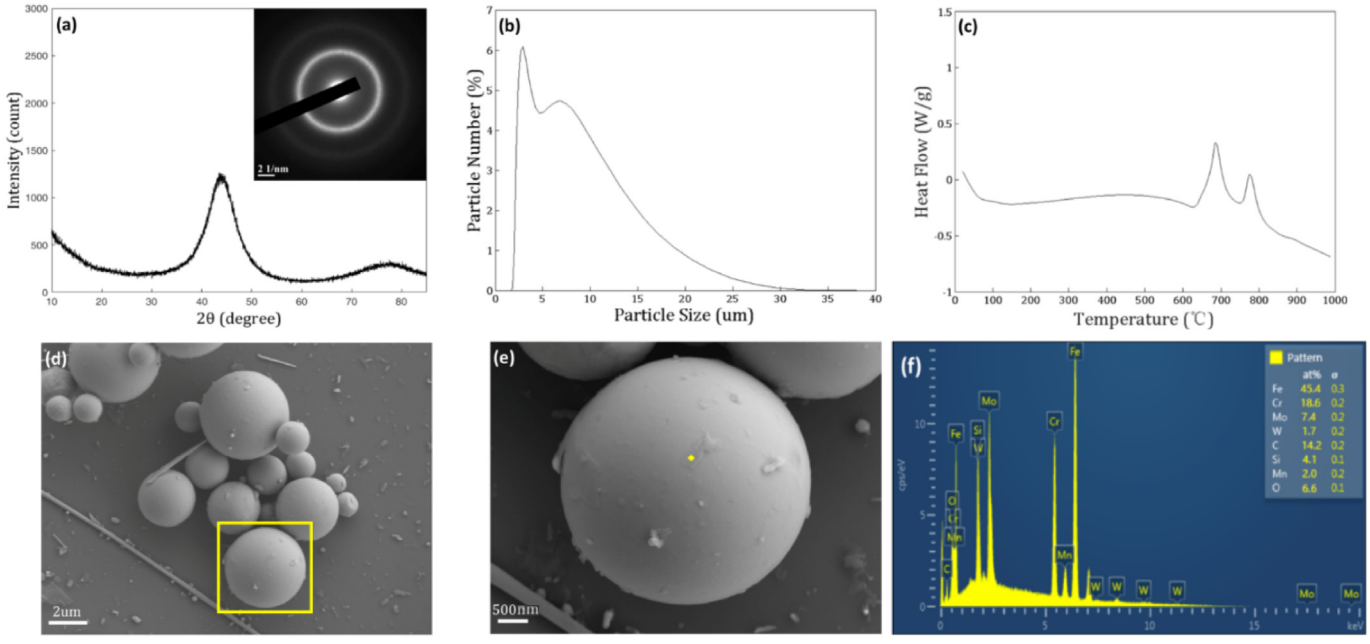


**Fig. 1.** Characterization of the as-received samples before the *in-situ* BCDI measurements. a) Powder X-ray diffraction (XRD) pattern of the Fe-based MG sample. The inset panel at the top-right corner is the selected area electron diffraction (SAED) pattern. b) Size distribution profile of the MG sample measured by a laser particle analyzer. c) Differential scanning calorimetry (DSC) measurement on the MG sample. d) Scanning electron microscope (SEM) micrograph of the MG sample. e) A zoomed-in SEM image of the yellow highlighted square region located near the bottom of the panel d. f) Energy dispersive spectrometer (EDS) measurement result at the point on an MG particle indicated by a yellow dot in panel e. (For interpretation of the references to colour in this figure legend, the reader is referred to the web version of this article.)

3.8 at.% C and 15.2 at.% B. The failure to record the B element is caused by the limitation of the capabilities of used EDS detector which cannot detect the characteristic X-ray signals from the B atoms.

### 3.2. Formation of nano-crystalline materials upon annealing

As there is generally only one crystal can be measured at a time during the BCDI experiments, and according to Köster et al. [39], the primary crystallization product of Fe-based MGs during heating is usually α-Fe, so we are aiming at recording the growth of the α-Fe crystals within the measured Fe-based MGs, and the detector was placed close to the (110) Bragg peak of the α-Fe crystal whose $2\theta = 39.7°$ at the chosen 9 keV X-rays.

Before starting the heating and the BCDI measurements, every sample was scanned along the (Bragg) 2θ angle between 10° and 70° to check the sample status, and as expected, only background scattering signals were recorded on the detector. One of these examples, where the centre of the detector was positioned at $2\theta = 39.5°$, is shown in Fig. S1 in the Supporting information (SI). In our BCDI set-up, the used Pilatus 100K detector will cover about 1° of 2θ angle which means Fig. S1 could record Bragg diffraction signals between 2θ equals about 39° and 40°. This confirms the amorphous nature of the starting sample again.

The as-received MG samples were then annealed in a vacuum chamber at the beamline I-07 at Diamond Light Source from room temperature at a base pressure of $2.10 \times 10^{-10}$ mbar while the BCDI measurements were carried out simultaneously. The samples were "rocking-curve" scanned [25,33] repeatedly within 1° range at the detector centering at $2\theta = 39.5°$ (around the α-Fe's Bragg peak) with 0.01° interval and 2 s exposure time or linearly scanned vertical to the X-ray beam route at the detector centering at $2\theta = 39.5°$ with 2 s exposure time as well in order to capture the gradual evolution of the formation of nano-crystalline materials under heating. There were two different heating processes used to treat the MG samples. They are denoted as heating process one (HP1) and heating process two (HP2), and shown as heating curves one and two in Fig. 2d. In the latter case, the structure evolution of crystals while cooling was recorded. Both heating processes, HP1 and HP2, were performed intentionally based on the DSC measurement result on the MG. To avoid missing the start point of the primary crystallization, during HP1, the MG sample was firstly heated to about 500°C with a lower heating rate, compared with 20 K/min, and then was heated to 704°C with a much lower rate, *i.e.* at a bit slower than 1 K/min. Based on the experience from HP1, during HP2, the MG sample was heated to about 500 °C quickly, then to about 585 °C with lower heating rate, and then very slowly to 625 °C to ensure to cover the first stage of crystallization.

The first α-Fe nano-crystal diffraction signals were captured after 10 h of heating during HP1 when the temperature reached 585°C. However, it took about 25 h (during HP1) until the Bragg peak from the growing crystals increased sufficiently for the Bragg diffraction signals

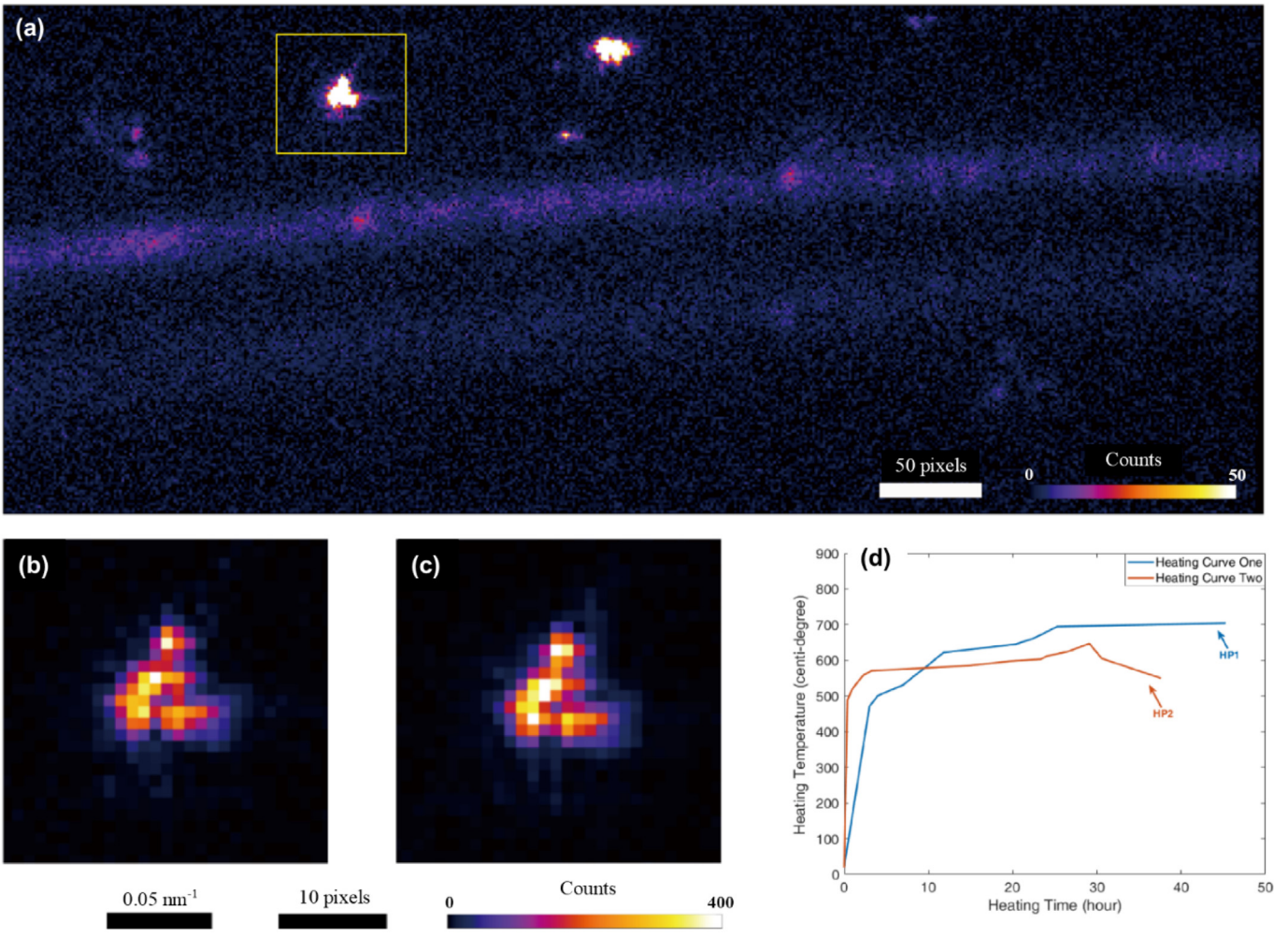


**Fig. 2.** Coherent X-ray diffraction patterns of the annealing MG recorded on a Pilatus detector. a) The diffraction pattern recorded on the detector that was centered at $2\theta = 39.2°$. A series of measurements on the same single Bragg peak was then carried out at different times; b) Zoomed-in image of the Bragg peak marked in a yellow square in panel a; c) Measurement made 20 min after panel b recorded; d) Two different heating processes (marked as HP1 and HP2) that the MG samples experienced in the *in-situ* BCDI experiments. (For interpretation of the references to colour in this figure legend, the reader is referred to the web version of this article.)

to become strong enough for the BCDI reconstruction to converge. Fig. 2a presents the diffraction pattern of the sample, which underwent HP1, captured at the detector centering at $2\theta = 39.2°$ after 40 h of heating when the temperature reached 704°C. Notably, there are bright diffraction spots recorded at higher angle on the detector that are the Bragg diffractions of the α-Fe from the (110) facet. By comparison, the diffraction pattern of the sample recorded at the end of HP2 is shown in Fig. S2, which records no such diffraction powder ring as shown in Fig. 2a, but only distinct Bragg diffraction spots. The observation of a continuous powder ring and more distinct diffraction spots resulting from HP1 than those resulting from HP2 suggests that there appear to be many more small crystals grown after HP1 treatment than HP2's. This means after longer time and higher temperature treatment (HP1), the crystallization degree of Fe-based MG goes higher. Fig. 2b is the zoomed-in image of the Bragg diffraction spot in the yellow-highlighted square in Fig. 2a. Fig. 2c shows subsequent measurements of this Bragg diffraction spot after 20 min of heating. The temperature was kept at 704°C while the above two measurements made.

These measured Bragg peaks were used to reconstruct the 3D images of the crystal using algorithms based on Error Reduction (ER) [40] and Hybrid Input-output (HIO) [41] methods.

### 3.3. Growth of crystals within the MG

The crystal formation was recorded in several MG samples. In Fig. 3, the growth of two individual α-Fe crystals is shown with their radial density functions (RDFs). In these images, the reconstructed amplitude was used to define the surfaces/shape of the shown crystals and the displacement was used to define the colour of the surfaces and interior. 25% of the maximum value of the reconstructed amplitude was chosen to render the crystal surfaces, and the presented crystals are the "core" crystalline regions. The above-mentioned rendering criterions are applied to the other crystals presented in this work as well.

During HP1, the Bragg peaks became strong enough to recover the images of the growing crystals at 704°C after 25 h of heating. The temperature was kept at 704°C after 25 h until the end of the heating process. In this period, the growth of one of the single α-Fe crystals was observed at the detector centering at $2\theta = 39.2°$. Fig. 3a and b show this crystal (named as crystal I) grain at two different times during the heating. As seen in Fig. 3a and a', the grain of crystal I has a cylindrical shape with some large phase values corresponding to displacements around its surface. These displacement fields can be quantified by the phase shift φ, formed by projection of the displacement onto the **Q** vector by the equation $\varphi = \mathbf{Q}\cdot\mathbf{u}$ [25]. The **Q** vector here is pointing to the (110) Bragg peak of the α-Fe crystal as denoted by the red arrows in the XYZ axes. The formal strain within the crystal can be estimated from the partial differentiation of **u** with respect to each direction [34]. A relative displacement of 0.069 nm is measured around the surface, and the scale bar is set to show the displaced region. The time interval between Fig. 3a and Fig. 3b is 20 min. After this time interval, several nodules develop at the edges of the crystal growing along its long sides, which become more elongated in the Z direction. The displacement fields within different regions, denoted by black arrows in the figures, are conserved in time, although the positions of the displacement fields change a bit. The magnitude of these fields also does not change over the period according to image reconstructions. This indicates that the displaced region does not change over time, which suggests that both the tensile and compressive strains within the crystal lattice were retained during crystal growth. The later formed nodules appear to have their displacement unchanged upon growth, which indicates a smooth connection between the newly formed nodule and the original grain. Additionally, all these nodules grew parallel to the Z axis that is parallel to the X-ray beam route, namely, parallel to the sample surface or the tangential direction to the surface of the sphere-shaped samples in our experiment. This indicates that the crystal has a preferential growth along the surface of the MG sample particles.

During HP2, the grown crystal (named as crystal II) was observed after the sample was heated for 28 h and had reached 625°C. Its Bragg diffraction was recorded at the detector positioning at $2\theta = 39.5°$, and the reconstructed images of crystal II are shown in Fig. 3c and c′. Crystal II shows a cuboid shape with negative displacement around the corner as pointed out in Fig. 3c and with positive displacement at the center of one facet as marked in Fig. 3c′. Crystal II was then heated to 647 °C for 40 min and measured again, and the result is shown in Fig. 3d and d′. There is a new fragment formed at the corner of the original crystal grain along the Z axis as well, and this new fragment has large negative displacements within it. This abrupt growth with unusual appearance may be caused by a preferential growth direction defined by the grown parts in the crystal which is also parallel to the Z axis. Another possibility is that there was already a new crystallized fragment near the original crystal, but due to the different orientations of the (110) facet between the two parts, the new one cannot be detected while the measurement was done for the reconstruction of Fig. 3c and c'. After 40 min of heating, the orientation of the new fragment changed and became close to that of the main one in Fig. 3c. It can also be seen that the domain of the positive displacement field, located at the center of the cuboid, decreased over the period. The maximum displacement has also decreased from 0.050 nm to 0.031 nm. Meanwhile, the negative displacement regions become larger over time, which suggests a compressive condition during crystal growth.

The radial density functions (RDFs) of crystals I and II are presented in Fig. 3e and f to help further explain the growth mechanism of the Fe-based MG. The RDF profile, the density appearing at a certain radius, was produced by evaluating the amplitude of crystal image density as a function of the radial distance from the center of mass, averaged over spherical shells. Two distinct slopes can be seen in the RDF profiles in Fig. 3e and f. The first slope, labeled as slope 1, is steeper and the radial distance to its ending point indicates the size of the core crystal region. While the second one, labeled as slope 2, shows a gentler slope, indicating that this region is out of the dense core region of the crystal [38]. The overwhelming majority of this outer region is not shown in the images in Fig. 3, which is a corona region formed by fractals. The RDF lines plotted in the outer region show the best fit of linear curves. The gradient of the second slope in crystal I increases from 0.32 to 1.13 over 20 min of heating, while in crystal II, it rises from 1.52 to 1.73 from the first to the second measurement. These gradient values match well with a cluster diffusion limited aggregation (CDLA) model and are denoted as fractal dimensions (FDs) [42,43]. The increase of FDs suggests the concentration of aggregate increased as well [42]. This means that the crystallization density is increasing at the inner boundary of the outer corona region in both crystals I and II. The microstructure of the outer regions is also becoming more complicated while the crystallization continues with heating.

Another example of α-Fe crystal growth is shown in the SI as Fig. S3.

Based on the discussion above, we suggest that the initial inner crystal grain grows larger over time while the density of the outer fractal corona keeps increasing. This proposes a two-step procedure for the growth of individual crystals from the MG: firstly, the core region of the crystal grain (with "full" density) forms and the outer corona region of fractal parts starts to grow; secondly, the outer fractal parts grow denser at the inner boundary of the corona region with an increasing crystallization density, and the inner boundary parts eventually become parts of the inner core region of the crystal grain.

This two-step procedure is different from the two-stage crystallization happened at 2 different temperatures as shown in Fig. 1c. The two-step procedure proposed here presents the crystal growth mechanism during individual crystallization processes in the Fe-based MGs during heating. However, the two-stage crystallization contains 2 different crystallization processes happened successively during heating, and the two-step procedure could happen at either of these 2 stages.

### 3.4. Growth stagnation and strain relaxation while cooling

In HP2, with a recorded cooling process, as shown in Fig. 2d, the sample reached a maximum temperature of 647°C after 29 h of heating, then lowered to 607°C over 1.5 h, and then further decreased to 550°C over 7 h. As displayed in Fig. 4, when the temperature was decreased, the α-Fe crystals stopped enlarging and showed internal strain relaxation while the crystal size changed a little. These 3D images of the crystal were reconstructed from Bragg diffraction recorded at the detector centering at $2\theta = 39.5°$ as well.

Fig. 4a and a′ show an α-Fe crystal (named as crystal III), captured at 598°C during the temperature decreasing period in HP2, which is given in two views from different orientations and one intermediate cut-through slice (Fig. 4a″). Regions of positive displacement can be seen on the facet of the crystal and around the corner, reaching a maximum of 0.034 nm. The strain distribution of an individual crystal is the gradient of displacement field thus there is a tensile strain between the positive displacement field and non-displacement field. The subsequent measurement results are shown in Fig. 4b (at 589°C) and 4c (at 581°C) that were carried out at 70 min and 140 min after the first measurement on crystal III. Over this series, the shape of crystal III had little change. Although the maximum value of the displacement field does not change, the area of displacement field shrinks in crystal III from Fig. 4a to c (marked by the black arrows). It can be further seen from the slices that positive displacement regions gradually shrink from the inner parts to the outer parts of the crystal grain (indicated by the red arrows). This can be understood as being due to structure relaxation of crystals while cooling, which reduces or annihilates the displacement within the inner crystal lattice first, not from the surface.

Despite the strain relaxing over time, there is minor variation over the surface region. Fig. 4d shows the RDFs of crystal III. The FDs of crystal III is keeping similar, ranging from 0.64 at the first to 0.79 at the third measurement which suggests that the microstructure of surface region in crystal III remains relatively stable over time. This agrees with the above discussion as well.

A second good example of an α-Fe crystal (named as crystal IV) displaying crystal growth stagnation and strain relaxation close to the end of HP2, while cooling, is shown as Fig. S4 in the SI. The result proves again that within the developing crystal grain the positive displacement regions gradually shrink from the inner parts to the outer parts.

### 3.5. Characteristics of the annealed specimens

The same MG material was annealed by the same heating process (as shown in HP2) in a digitally controlled vacuum oven, and this annealed MG material was then measured by a powder X-ray diffractometer. It gives the result shown in Fig. 5a. Additionally, after the *in-situ* BCDI measurements by X-rays at the beamline, the annealed samples were removed from the vacuum chamber and then measured by SEM (see Fig. 5b–h).

Compared with the XRD result of raw powders in Fig. 1a, the annealed samples experienced HP2 have new crystalline peaks, identified mainly

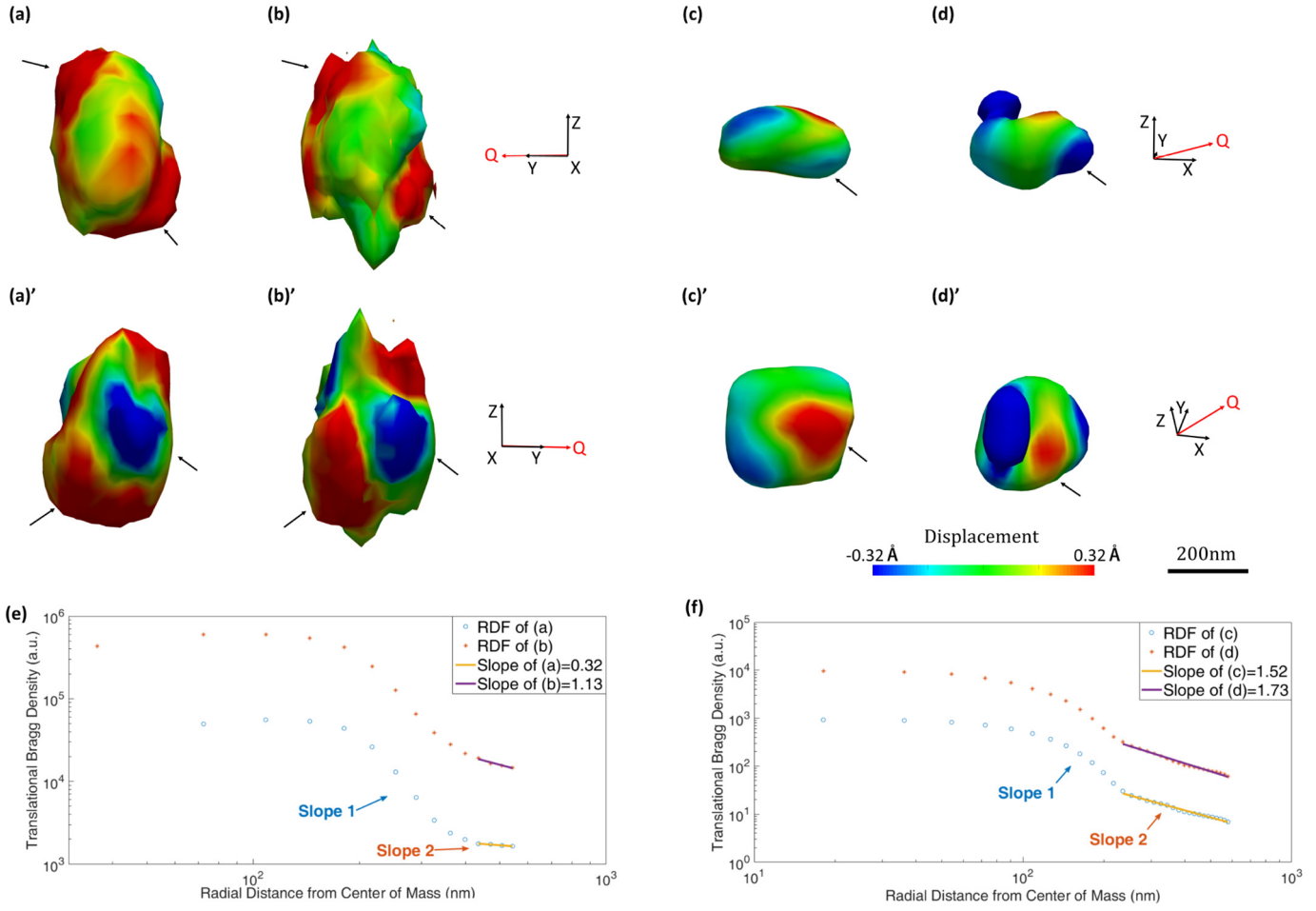


**Fig. 3.** α-Fe crystal growth upon heating. a) & a′) Reconstructed images of crystal I that was heated to 704°C (experienced HP1) in two views from different orientations. b) & b′) Images of crystal I, kept heating at 704°C, acquired 20 min after panel a was measured. c) & c′) Reconstructed images of crystal II that was heated to 625°C (experienced HP2) in two views from different orientations. d) & d′) Images of crystal II that was heated at 647°C and acquired 40 min after panel c was measured. e) The radial density functions (RDFs) of crystal I. f) The RDFs of crystal II. Black arrows in panels 3a to 3d′ mark the displacement regions on the surface of the crystals. 3D images of crystals I and II were reconstructed from Bragg diffraction recorded under 9 keV X-ray illumination at the detector centering at $2\theta = 39.2°$ during HP1 (panels a & b) and at the detector centering at $2\theta = 39.5°$ during HP2 (panels c & d).

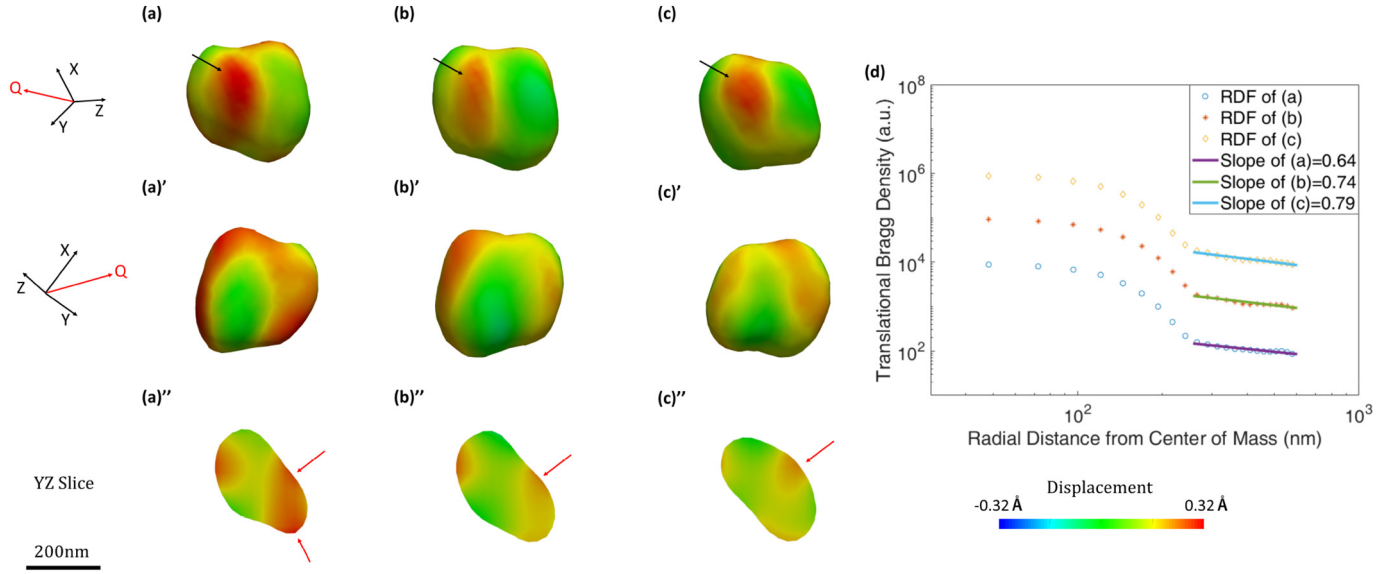


**Fig. 4.** Growth stagnation and strain relaxation in the α-Fe crystal III when temperature is decreased (in HP2). a) & a′) Reconstructed images of the crystal in two views from different orientations when first measured at 598°C. b) & b′) Reconstructed images of the same crystal 70 min after the first measurement (shown in panel a) at 589°C. c) & c′) Measurement of the same crystal made 140 min after the first measurement at 581°C. a″), b″) & c″) Intermediate cut-through slices of the reconstructed 3D images of the crystal III in panels a, b and c. d) RDFs of the crystal III as shown in panels a, b and c. Black and red arrows mark the residual strain in the crystal. The left-side 3D images of crystals III were reconstructed from Bragg diffraction recorded at the detector centering at $2\theta = 39.5°$. (For interpretation of the references to colour in this figure legend, the reader is referred to the web version of this article.)

as α-Fe, $Cr_{23}C_6$, $Fe_2C$ and $Fe_3B$. Fig. 5b shows an SEM micrograph of the MG sample that experienced HP2 treatment, and Fig. 5c is a zoomed-in image which shows the annealed spherical MG particle. Compared with the raw powders in Fig. 1e, many surface protrusions have appeared, scattered all over the surface of the annealed particle. Fig. 5d is a zoomed-in SEM micrograph of one of these surface protrusions, in Fig. 5c, which displays well-defined shapes suggesting they probably are crystals. Some more of these protrusions on the same annealed MG particle in Fig. 5c are present in Fig. S5 in the SI. These protrusions appear after the HP2 treatment and have well-defined shapes. They should be the crystallization products. The sizes of these newly-formed protrusions are between 200 nm (see Fig. S5b) and 520 nm (see Fig. 5d), roughly the same as that of the BCDI images discussed above. Furthermore, Fig. 5e shows the SEM micrograph obtained from the samples that experienced HP1 treatment with further zoomed-in images shown in Fig. 5f to h. Fig. 5f is the zoomed-in SEM micrograph of the high-lighted upper area in Fig. 5e, which shows a part of an annealed particle covered by many surface protrusions as well. However, these protrusions have much less well-defined shapes than those in Fig. 5d and S5, which is consistent with the results in Fig. 3a and b. They also have broader size distribution as well. Fig. 5g, a zoomed-in SEM micrograph of the high-lighted lower area in Fig. 5e, shows another sphere with a porous structure all over the surface. Fig. 5h, which is the zoomed-in image of the high-lighted middle area in Fig. 5e, captures a sphere with both morphologies that appeared in the above 2 images, with the right part covered in surface protrusions and the left part with a porous surface but without protrusions. These spherical particles with a porous surface appear to be connected with HP1 treatment only and cannot be seen in raw powders or samples

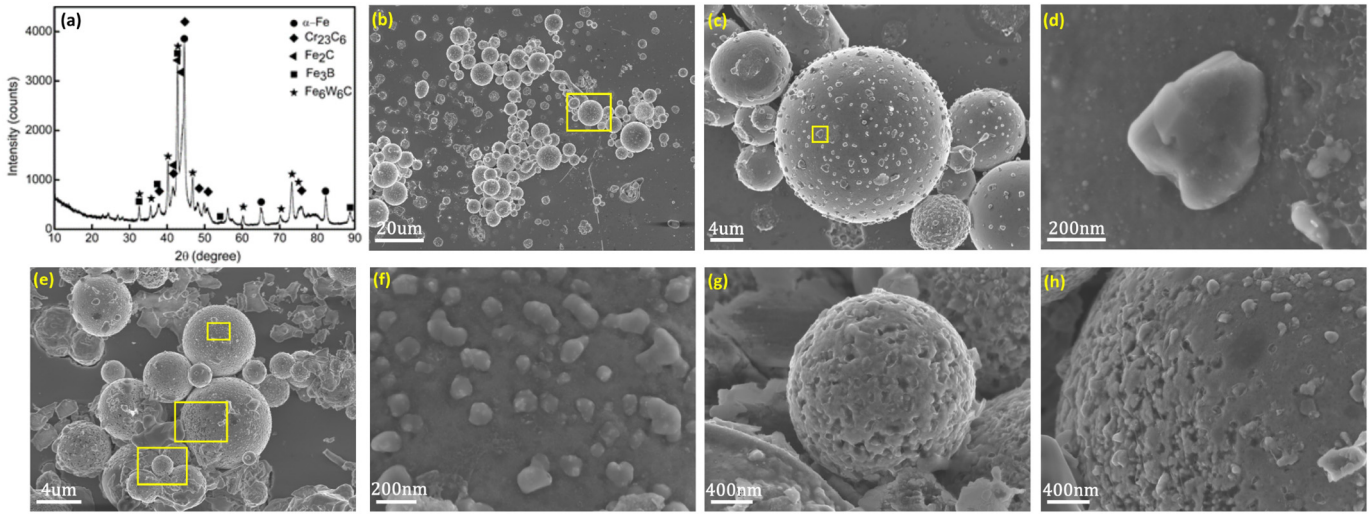


**Fig. 5.** Characterization of the MG samples after annealing. a) Powder XRD pattern of the heated MG sample which have experienced HP2 treatment. b) SEM micrograph of the MG powders after HP2 treatment (and the BCDI measurements). c) A zoomed-in image of the yellow square region in panel b. d) A zoomed-in image of the yellow square region in panel c. e) SEM micrograph of the MG powders after HP1 treatment (and the BCDI measurements). f), g) & h) Three zoomed-in images of the yellow square highlighted upper, lower and middle regions in panel e. (For interpretation of the references to colour in this figure legend, the reader is referred to the web version of this article.)

after HP2 treatment. A similar example to the sample in Fig. 5e to 5h was shown in Fig. S6 in the SI.

It could be assumed that the above-mentioned surface protrusions with well-defined shapes in Fig. 5c, d and S5 are the products of the primary crystallization of α-Fe which forms the first exothermic DSC peak in Fig. 1c at lower temperature (in HP2). These protrusions could then transform into crystals with less well-defined shape and formed the porous structure in the annealed MG particles at a higher heating temperature (in HP1). Additionally, from both the BCDI and SEM measurements, the identified crystal grains resulting from lower temperature annealing (see crystals in Figs. 3c, 4, 5d and S4) have much better-defined shapes than those from higher temperature treatment (see crystals in Figs. 3a, b, 5f and S3). This indicates that during the crystallization of Fe-based MGs, the α-Fe crystal could be generated first at lower temperature, while the temperature goes higher, the α-Fe crystals could transform into crystals with less well-defined shape probably through invasion by other elements, *i.e.* the α-Fe crystals are eroded by other atoms such as C, B or Cr at higher temperature and make them into less well-defined shapes. This indicates that at higher temperature after the first exothermic DSC peak in Fig. 1c, the crystallization of α-Fe in the Fe-based MGs could be a competition process between the growth of α-Fe crystals and the erosion from other elements.

Additionally, with the increase of the crystallization degree of the MG sample under high-temperature and long-time HP1 treatment, as discussed above, the density difference among the lighter raw MG material (measured to be 7.701 g/cm$^3$), the light $Cr_{23}C_6$ crystalline phase (7.07 g/cm$^3$) and the main and heavier α-Fe crystalline phase (7.845 g/cm$^3$) could cause the relative volume shrinkage of the measured samples, and then cause formation of the porous structure of the MG samples after HP1 treatment with the help of the possible evaporation of materials from the MG in high vacuum as shown in Fig. 5g and h. This way, crystallizing amorphous materials through annealing, could be a method to produce porous alloy in future as well.

## 4. Conclusions

In summary, *in-situ* BCDI experiments were performed on Fe-based MG samples during annealing in a vacuum environment with the annealing temperature in the vicinity of the crystallization transition to observe the formation of nano-crystallites.

Upon heating, the growth of α-Fe crystals was observed, which formed nodules that subsequently filled in. Their RDFs suggest the possibility of fractal structure in the outer regions of the crystals and the progressive increase of their FDs indicate density compaction during crystallization of their outer corona. There is also preferential growth along the surface of the MG particles during the crystallization. A two-step model is proposed to describe the growth of individual crystals in the MG samples during heating. Firstly, the core part of the crystal grain (with "full" density) forms and the outer corona region of fractal parts grows. Secondly, the outer fractal regions grow denser at the inner boundary of the corona region and eventually become parts of the crystal grain core from inner sides. The results also suggest that at the temperature higher than the first exothermic DSC peak of the targeted Fe-based MGs, there could be a competition process between the growth of α-Fe crystals and the erosion from other elements during the crystallization of α-Fe. While decreasing the temperature after heating, the crystals were found to stop changing shape, and the displacement fields gradually diminish from the inner parts to the surfaces of the crystals, which presents strain relaxation upon cooling within the crystals.

Additionally, The BCDI and SEM measurements are complementary in this work. The annealed samples show that regularly distributed crystal grains with well-defined shapes with sizes of 200 nm to 520 nm are formed around the surface of MG particles after annealing at lower temperature. These crystals are believed to be the grown α-Fe crystals that are the products of primary crystallization of the Fe-based MGs. On the other hand, as the crystallization degree increases after higher temperature and long-time treatment, the relative volume shrinkage among the lower density parts and the higher density α-Fe crystalline phase leads to the formation of the porous structure in the annealed MG specimens.

## Declaration of competing interest

The authors declare that they have no known competing financial interests or personal relationships that could have appeared to influence the work reported in this paper.

## Acknowledgments

This work was supported by the "Shanghai PuJiang Talent Program" with grant no. 18PJ1410400, and the High-level Talent Program "Materials Nano-structure" of Tongji University, China, with grant nos. 152221 and 152243, and the EPSRC-UK grant "Phase modulation technology for X-ray imaging" with no. EP/I022562/1. The work was also partially supported by the National Natural Science Foundation of China with grant nos. 51971160, 51971061 and 51601130. The BCDI experiments were carried out at the Beamline I-07 at the Diamond Light Source, UK. We thank Dr. Xiaowen Shi for assistance with the BCDI measurements.

## Author contributions

B.C., Q.L., J.S. and I. R. conceived the project. Q.L. and J.S. prepared the MG samples and performed the TEM measurement. B.C., J.D., J.R., X.L., C.N. and I.R. carried out the *in-situ* BCDI experiment. B.C., J.D. and Q.L. analyzed the BCDI data. J.D., Q.L. and B.C. carried out the DSC and powder XRD measurements. B.C., Q.L. and J.D. performed SEM measurements. B.C., J.D. and I.R. wrote the manuscript with contributions from all the other co-authors.

## Data and materials availability

All data needed to evaluate the conclusions in the paper are present in the paper and/or the Supplementary Materials. Additional data related to this paper are available from the corresponding authors upon reasonable requests.

## Appendix A. Supplementary data

Supplementary data to this article can be found online at https://doi.org/10.1016/j.matdes.2020.108551.

## References

[1] F. Zhu, S. Song, K.M. Reddy, A. Hirata, M. Chen, Spatial heterogeneity as the structure feature for structure–property relationship of metallic glasses, Nat. Commun. 9 (2018) 3965.
[2] N. Li, J. Zhang, W. Xing, D. Ouyang, L. Liu, 3D printing of Fe-based bulk metallic glass composites with combined high strength and fracture toughness, Mater. Design 143 (2018) 285–296.
[3] S. Lan, Z. Wu, X. Wei, J. Zhou, Z. Lu, J. Neuefeind, X. Wang, Structure origin of a transition of classic-to-avalanche nucleation in Zr-Cu-Al bulk metallic glasses, Acta Mater. 149 (2018) 108–118.
[4] F. Zhu, A. Hirata, P. Liu, S. Song, Y. Tian, J. Han, T. Fujita, M. Chen, Correlation between local structure order and spatial heterogeneity in a metallic glass, Phys. Rev. Lett. 119 (2017), 215501.
[5] R.V. Sundeev, A.M. Glezer, A.P. Menushenkov, A.V. Shalimova, O.V. Chernysheva, N.V. Umnova, Effect of high pressure torsion at different temperatures on the local atomic structure of amorphous Fe-Ni-B alloys, Mater. Des. 135 (2017) 77–83.
[6] S. Sohn, Y. Xie, Y. Jung, J. Schroers, J.J. Cha, Tailoring crystallization phases in metallic glass nanorods via nucleus starvation, Nat. Commun. 8 (2017) 1980.
[7] S. Sohn, Y. Jung, Y. Xie, C. Osuji, J. Schroers, J.J. Cha, Nanoscale size effects in crystallization of metallic glass nanorods, Nat. Commun. 6 (2015) 8157.
[8] A. Inoue, B.L. Shen, H. Koshiba, H. Kato, A.R. Yavari, Cobalt-based bulk glassy alloy with ultrahigh strength and soft magnetic properties, Nat. Mater. 2 (2003) 661–663.

[9] R. Yamada, Y. Shibazaki, Y. Abe, W. Ryu, J. Saida, Unveiling a new type of ultradense anomalous metallic glass with improved strength and ductility through a high-pressure heat treatment, NPG Asia Mater 11 (2019) 72.
[10] J. Schroers, Processing of bulk metallic glass, Adv. Mater. 22 (2010) 1566–1597.
[11] M.T. Clavaguera-Mora, N. Clavaguera, D. Crespo, T. Pradell, Crystallisation kinetics and microstructure development in metallic systems, Prog. Mater. Sci. 47 (2002) 559–619.
[12] R. Maa, J.F. Loffler, Shear-band dynamics in metallic glasses, Adv. Funct. Mater. 25 (2015) 2353–2368.
[13] W.H. Wang, Bulk metallic glasses with functional physical properties, Adv. Mater. 21 (2009) 4524–4544.
[14] W.H. Wang, C. Dong, C.H. Shek, Bulk metallic glasses, Mater. Sci. Eng. R 44 (2004) 45–89.
[15] M. Shapaan, J. Gubicza, J. Lendvai, L.K. Varga, Crystallization behavior of $(Fe_{100-x}Co_x)_{(62)}Nb_8B_{30}$ bulk amorphous alloy, Mater. Sci. Eng. A 375 (2004) 785–788.
[16] H. Chen, Y. He, G.J. Shiflet, S.J. Poon, Mechanical-properties of partially crystallized aluminum based metallic glasses, Scripta Mater 25 (1991) 1421–1424.
[17] J. Basu, N. Nagendra, Y. Li, U. Ramamurty, Microstructure and mechanical properties of a partially crystallized La-based bulk metallic glass, Philos. Mag. 83 (2003) 1747–1760.
[18] H.N. Chapman, K.A. Nugent, Coherent lensless X-ray imaging, Nat. Photonics 4 (2010) 833–839.
[19] J. Miao, P. Charalambous, J. Kirz, D. Sayre, Extending the methodology of X-ray crystallography to allow imaging of micrometre-sized non-crystalline specimens, Nature 400 (1999) 342–344.
[20] I.K. Robinson, I.A. Vartanyants, G.J. Williams, M.A. Pfeifer, J.A. Pitney, Reconstruction of the shapes of gold nanocrystals using coherent X-ray diffraction, Phys. Rev. Lett. 87 (2001), 195505.
[21] J.M. Rodenburg, A.C. Hurst, A.G. Cullis, B.R. Dobson, F. Pfeiffer, O. Bunk, C. David, K. Jefimovs, I. Johnson, Hard-X-ray lensless imaging of extended objects, Phys. Rev. Lett. 98 (2007), 034801.
[22] M. Dierolf, A. Menzel, P. Thibault, P. Schneider, C.M. Kewish, R. Wepf, O. Bunk, F. Pfeiffer, Ptychographic X-ray computed tomography at the nanoscale, Nature 467 (2010) 436–439.
[23] F. Zhang, B. Chen, G.R. Morrison, J. Vila-comamala, M. Guizar-sicairos, I.K. Robinson, Phase retrieval by coherent modulation imaging, Nat. Commun. 7 (2016), 13367.
[24] K. Wakonig, A. Diaz, A. Bonnin, M. Stampanoni, A. Bergamaschi, J. Ihli, M. Guizar-Sicairos, A. Menzel, X-ray Fourier ptychography, Sci. Adv. 5 (2019) eaav0282.
[25] I.K. Robinson, R. Harder, Coherent X-ray diffraction imaging of strain at the nanoscale, Nat. Mater. 8 (2009) 291–298.
[26] D. Karpov, E. Fohtung, Bragg coherent diffractive imaging of strain at the nanoscale, J. Appl. Phys. 125 (2019), 121101.
[27] G. Xiong, J.N. Clark, C. Nicklin, J. Rawle, I.K. Robinson, Atomic diffusion within individual gold nanocrystal, Sci. Rep. 4 (2014) 6765.
[28] Y.K. Chen-Wiegart, R. Harder, D.C. Dunand, I. McNulty, Evolution of dealloying induced strain in nanoporous gold crystals, Nanoscale 9 (2017) 5686.
[29] A. Ulvestad, A. Singer, J.N. Clark, H.M. Cho, J.W. Kim, R. Harder, J. Maser, Y.S. Meng, O.G. Shpyrko, Topological defect dynamics in operando battery nanoparticles, Science 348 (2015) 1344–1347.
[30] A. Ulvestad, A. Singer, H.M. Cho, J.N. Clark, R. Harder, J. Maser, Y.S. Meng, O.G. Shpyrko, Single particle nanomechanics in operando batteries via lensless strain mapping, Nano Lett. 14 (2014) 5123–5127.
[31] X. Liu, W. Lin, B. Chen, F. Zhang, P. Zhao, A. Parsons, C. Rau, I. Robinson, Coherent diffraction study of calcite crystallization during the hydration of tricalcium silicate, Mater. Des. 157 (2018) 251–257.
[32] J.N. Clark, J. Ihli, A.S. Schenk, Y.Y. Kim, A.N. Kulak, J.M. Campbell, G. Nisbet, F.C. Meldrum, I.K. Robinson, Three-dimensional imaging of dislocation propagation during crystal growth and dissolution, Nat. Mater. 14 (2015) 780–784.
[33] M.A. Pfeifer, G.J. Williams, I.A. Vartanyants, R. Harder, I.K. Robinson, Three-dimensional mapping of a deformation field inside a nanocrystal, Nature 442 (2006) 63–66.
[34] M.C. Newton, S.J. Leake, R. Harder, I.K. Robinson, Three-dimensional imaging of strain in a single ZnO nanorod, Nat. Mater. 9 (2010) 120–124.
[35] C. Zhang, L. Liu, K.C. Chan, Q. Chen, C.Y. Tang, Wear behavior of HVOF-sprayed Fe-based amorphous coatings, Intermetallics 29 (2012) 80–85.
[36] K. Chokethawai, D.G. McCartney, P.H. Shipway, Microstructure evolution and thermal stability of an Fe-based amorphous alloy powder and thermally sprayed coatings, J. Alloy Compd. 480 (2009) 351–359.
[37] T. Koziel, A. Zielinska-Lipiec, Z. Kedzierski, T. Czeppe, Transmission electron microscopy study of crystallization in Fe-Si–B–Cr–C amorphous alloy, J. Microsc. 224 (2006) 27–29.
[38] J. Diao, B. Chen, Q. Luo, W. Lin, X. Liu, J. Shen, I. Robinson, Nucleation of fractal nanocrystallites upon annealing of Fe-based metallic glass, J. Mater. Res. 32 (2017) 1880–1887.
[39] U. Köster, U. Harold, Glassy Metals I, Springer-Verlag, Berlin, Germany, 1981.
[40] J.R. Fienup, Reconstruction of an object from modulus of its fourier-transform, Opt. Lett. 3 (1978) 27–29.
[41] J.R. Fienup, Phase retrieval algorithms - a comparison, Appl. Opt. 21 (1982) 2758–2769.
[42] T.A. Witten, L.M. Sander, Diffusion-limited aggregation, a kinetic critical phenomenon, Phys. Rev. Lett. 47 (1981) 1400–1403.
[43] P. Meakin, Z.R. Wasserman, Some universality properties associated with the cluster cluster aggregation model, Phys. Lett. A 103 (1984) 337–341.